Kinetic energy and enstrophy transfer in compressible Rayleigh–Taylor turbulence

Zhiye Zhao[1], Nan-Sheng Liu[1] and Xi-Yun Lu[1],†

[1]Department of Modern Mechanics, University of Science and Technology of China, Hefei, Anhui 230026, PR China

Kinetic energy and enstrophy transfer in compressible Rayleigh–Taylor (RT) turbulence were investigated by means of direct numerical simulation. It is revealed that compressibility plays an important role in the kinetic energy and enstrophy transfer based on analyses of transport and large-scale equations. For the generation and transfer of kinetic energy, some findings have been obtained as follows. The pressure-dilatation work dominates the generation of kinetic energy in the early stage of flow evolution. The baropycnal work and deformation work handle the kinetic energy transfer from large to small scales on average for RT turbulence. The baropycnal work is mainly responsible for the kinetic energy transfer on large scales, and the deformation work for the kinetic energy transfer on small scales. The baropycnal work is also disclosed to be related to the compressibility from the finding that the expansion motion enhances the positive baropycnal work and the compression motion strengthens the negative baropycnal work. For the generation and transfer of enstrophy, the horizontal enstrophy is generated by the baroclinic effect and the vertical enstrophy by vortex stretching and tilting. Then the enstrophy is strengthened by the vortex stretching and tilting during the evolution of RT turbulence and the vorticity tends to be isotropic in the turbulent mixing region. The large-scale enstrophy equation in compressible flow has also been derived to deal with the enstrophy transfer. It is identified that the enstrophy is transferred from large to small scales on average and tends to stabilize for RT turbulence.

Key words: buoyancy-driven instability, compressible turbulence, turbulent mixing

1. Introduction

Rayleigh–Taylor instability (RTI) occurs as a consequence of potentially unstable superposition of a heavy fluid above a lighter one subjected to a sustained acceleration opposite to the density gradient (Youngs 1984, 1991). The RTI and its induced Rayleigh–Taylor (RT) turbulence are of great scientific interest in various physical respects, ranging on a broad scale from quantum plasma (Momeni 2013) to interstellar gas and galaxy clusters (Zweibel 1991; Novak, Ostriker & Ciotti 2011; Caproni *et al.* 2015); and also of critical industrial importance in extensive applications, such as premixed combustion (Chertkov, Lebedev & Vladimirova 2009), formation of the 'hot spot' in

† Email address for correspondence: xlu@ustc.edu.cn

inertial confinement fusion (Bodner *et al.* 1998; Besnard 2007) and aerosols (Hinds *et al.* 2002). As a canonical problem of non-stationary and non-isotropic turbulence, it provides a fascinating fluid mechanical framework to study the flow evolution to turbulence and the decaying turbulence with full-scale energy injection due to gravity. Therefore, efforts have been dedicated to incompressible RT flows in terms of theoretical analysis, experimental measurements and high-fidelity simulations, as reviewed recently by Boffetta & Mazzino (2017) and Zhou (2017*a*,*b*). However, the physical mechanisms dictating the characteristics of kinetic energy and enstrophy transfer in compressible RT turbulence are still unclear and are of great interest for further detailed studies.

Budget analyses of kinetic energy and enstrophy transfer in incompressible RT flows have been carried out to examine the generation, transfer and dissipation of kinetic energy and enstrophy. Cook & Zhou (2002) numerically investigated the energy budget for the incompressible RTI and noticed that the production and dissipation become increasingly opposite as the flow evolves. Cabot & Cook (2006) studied the global kinetic energy budget for the incompressible RT flows of two miscible fluids and found that the kinetic energy is converted from potential energy and balanced by viscous dissipation. Cabot (2006) dealt with two- and three-dimensional planar, miscible incompressible RT flows and identified that the baroclinicity acts as the dominant mechanism for the generation of enstrophy at the initial stage and the vortex-stretching term becomes mechanistically dominant at the late stage. Recently Zhou *et al.* (2016) also studied the scale-to-scale transport of kinetic energy, thermal energy and enstrophy in incompressible two-dimensional RT flows and revealed an inverse cascade of kinetic energy from small to large scales and a forward cascade of mean enstrophy from large towards small scales.

The influences of density stratification on RTI flows have been well studied and the relevant results are helpful in the understanding of the behaviours of compressible RT flows. George & Glimm (2005) improved previous density renormalizations to allow a unified treatment of compressible density stratification and mass diffusion in a range of weakly to strongly compressible multimode RT simulations. Jin *et al.* (2005) developed an analytical model accounting for the density stratification effects which are dominant in multimode self-similar mixing. Lafay, Le Creurer & Gauthier (2007) showed that increasing density stratification always stabilizes the RT flow and weakens vorticity production due to the baroclinic effect. Furthermore, Reckinger, Livescu & Vasilyev (2012) and Reckinger, Livescu & Vasilyev (2016) revealed that background stratification can either suppress or enhance the growth of RTI, depending upon the molar mass ratio of the pure fluids. Recently Wieland *et al.* (2019) also found that the stratification effect slows down the two-dimensional RTI evolution by a re-acceleration for weaker stratification and by a continuous suppression of RTI growth for stronger stratification.

The influence of flow compressibility on the behaviours of RT flows has been investigated in terms of dilatational and acoustic effects. Mellado, Sarkar & Zhou (2005) examined the compressibility effects in RT turbulence in an unbounded domain and indicated that limited compressibility effects occur with a turbulent Mach number of 0.25–0.6. Olson & Cook (2007) investigated RTI with the formation of shock waves due to the rising bubbles acting like pistons to continuously compress the upper heavy fluid and demonstrated a strong dilatation effect on the RTI flows. Le Creurer & Gauthier (2008) determined four regimes along the transition pathway for a two-dimensional single-mode compressible RTI, appearing in sequence as linear, nonlinear steady bubble rise, return towards equilibrium and finally acoustic waves. The final regime is damped by physical viscosity and also by thermal conduction. Gauthier (2017) also employed the Kovàsznay-mode decomposition to reveal great flow compressibility effects on the density and temperature fields via acoustic and entropic modes.

Studies of the dynamics of energy and enstrophy in compressible RT turbulence are still limited. Nevertheless, some interesting behaviours have been reported recently. Gauthier (2017) found that the velocity field spectra have a persistent anisotropy at all scales, as opposite to the Boussinesq case where intermediate scales are clearly isotropic while small scales are anisotropic. However, the concentration and temperature spectra also exhibit intermediate-scale isotropy and small-scale anisotropy, consistent with the Boussinesq RT turbulence. Moreover, vertical baroclinic vorticity production occurs, which vanishes for the incompressible case. Wieland *et al.* (2019) found that the dilatation effects also have an important influence on the evolution of vorticity for the compressible RTI, such as total baroclinic effects. They also revealed that bubble and spike asymmetries in RTI growth were formed as a consequence of the dilatation and stratification contributions to the baroclinic torque based on the analysis of the vorticity transport equation. These behaviours indicate that the generation and transfer of energy and entrophy for compressible RT turbulence include intriguing mechanisms which are desirable to be studied.

In the present study, the generation and transfer of kinetic energy and enstrophy in three-dimensional compressible RT turbulence are investigated by means of direct numerical simulation. The flow compressibility effects on the underlying mechanisms are mainly studied. The rest of this paper is organized as follows. The governing equations and numerical method are briefly given in § 2. The generation and transfer of kinetic energy are discussed in § 3. The generation and transfer of enstrophy are analysed in § 4. Finally, concluding remarks are presented in § 5.

2. Problem statement and numerical details

2.1. *Governing equations*

Compressible RT turbulence is started from the hydrostatic equilibrium of a layer of heavy fluid on top of a layer of lighter fluid, for which direct numerical simulation has been carried out by solving the mass, momentum and energy equations. We employ the initial pressure (p_I) and density (ρ_I) at the heavy fluid–light fluid interface as characteristic scales, where $\rho_I = (\rho_1 + \rho_2)/2$ with ρ_1 and ρ_2 being the densities at the upper and lower surfaces of the initial interface. Then a characteristic temperature is represented as $T_I = p_I/(R\rho_I)$, with R being the perfect gas constant, and a characteristic velocity as $U_I = \sqrt{p_I/\rho_I}$. The vertical length (L_z) of the flow domain is chosen as the characteristic length. Accordingly, the non-dimensionalized governing equations are given as

$$\frac{\partial \rho}{\partial t} + \frac{\partial (\rho u_i)}{\partial x_i} = 0, \tag{2.1}$$

$$\frac{\partial (\rho u_i)}{\partial t} + \frac{\partial (\rho u_i u_j)}{\partial x_j} = -\frac{\partial p}{\partial x_i} + \frac{1}{Re}\frac{\partial \tau_{ij}}{\partial x_j} - \frac{1}{Fr}\rho \delta_{i3}, \tag{2.2}$$

$$\frac{\partial (\rho e)}{\partial t} + \frac{\partial (\rho e + p)u_i}{\partial x_i} = \frac{1}{Re}\frac{\partial (u_i \tau_{ij})}{\partial x_j} + \frac{1}{RePr}\frac{\partial}{\partial x_i}\left(\frac{\partial T}{\partial x_i}\right) - \frac{1}{Fr}\rho u_3, \tag{2.3}$$

where ρ is the fluid density, u_i ($i = 1, 2$ and 3) is the velocity component in the x_i direction, or $(u_1, u_2, u_3) = (u, v, w)$ in $(x_1, x_2, x_3) = (x, y, z)$, p is the pressure, T is the temperature and e denotes the specific total energy obtained as $e = T/(\gamma - 1) + u_i u_i/2$ with the ratio

of specific heat $\gamma = 1.4$. The viscous stress τ_{ij} is represented as

$$\tau_{ij} = \mu \left(\frac{\partial u_i}{\partial x_j} + \frac{\partial u_j}{\partial x_i} \right) - \frac{2}{3} \mu \theta \delta_{ij}, \tag{2.4}$$

where $\theta = \partial u_k / \partial x_k$ is the dilatation related to the compression/expansion motions of fluid parcels and $\mu = T^{3/2}(1 + c)/(T + c)$ is the viscosity computed by the Sutherland law with $c = 110/T_r$ and the reference temperature T_r. The above governing equations are closed with the equation of state of an ideal gas, i.e. $p = \rho T$.

The non-dimensional parameters in the governing equations (2.1)–(2.3) are the Reynolds, Froude and Prandtl numbers defined as

$$Re = \frac{\rho_I U_I L_z}{\mu_I}, \quad Fr = \frac{U_I^2}{L_z g} \quad \text{and} \quad Pr = C_p \frac{\mu_I}{\kappa}, \tag{2.5a–c}$$

respectively, where g is the gravitational acceleration imposed opposite to the vertical direction, C_p the specific heat at constant pressure and κ the thermal conductivity.

2.2. *Numerical simulations*

Both the heavy and lighter layers are initialized as the buoyancy-stable configuration, which is indicated to have considerable flow compressibility effects (Mellado *et al.* 2005). Specifically, the heavy fluid is set at uniform temperature $T_{up} = 1/(1 - At)$ above the interface ($z > 0$) and the lighter fluid at $T_{low} = 1/(1 + At)$ below the interface ($z < 0$), where the Atwood number At is defined as

$$At = \frac{\rho_1 - \rho_2}{\rho_1 + \rho_2}. \tag{2.6}$$

Correspondingly, the hydrostatic equilibrium state is obtained from the governing equations (2.1)–(2.3) by setting u_i to be zero for a stationary solution. This solution is a potentially unstable stack of two stable exponentially stratified profiles:

$$\rho = (1 + At) \exp \left(-\frac{1 + At}{Fr} z \right) H^+(z) + (1 - At) \exp \left(-\frac{1 - At}{Fr} z \right) H^-(z), \tag{2.7}$$

where $H(z)$ is the Heaviside step function, and its upper symbols $+$ and $-$ represent the upper and lower side of the interface, respectively. The interface at $z = 0$ is perturbed by a superposition of cosine waves along the horizontal directions, i.e. $A_m \cos(2\pi k_x x/L_x + \phi_k) \cos(2\pi k_y y/L_y + \psi_k)$, where the perturbation wavenumbers k_x and k_y in the x and y directions are set in a range of $30 \leq k_x$ (or k_y) ≤ 60 with the amplitude $A_m = 10^{-4}$ and random phases ϕ_k and ψ_k (Clark 2003; Boffetta *et al.* 2009; Qiu, Liu & Zhou 2014).

In order to generate strong turbulence (Dimotakis 2000; Cabot & Cook 2006; Cabot & Zhou 2013), we use a high Atwood number of $At = 0.6$ (Bian *et al.* 2020) with $Re = 10^5$. The Froude number is fixed at $Fr = 1$. The RT flow is considered as homogeneous in the horizontal directions and thus periodic boundary conditions are used. There is no mass and heat flux through the top and bottom boundaries (Gauthier 2017). The computational domain is set as $L_x \times L_y \times L_z = 0.5 \times 0.5 \times 1$ in the x, y and z (vertical) directions, respectively. It is resolved by uniform grids of size $650 \times 650 \times 1300$. Similar to the numerical schemes used by Zhou, Zhang & Tian (2018) and Li *et al.* (2019), the seventh-order finite difference WENO scheme is implemented to discretize the convective

terms (Jiang & Shu 1996) and the eighth-order central difference scheme to discretize the viscous terms. The time derivative is approximated by the standard third-order Runge–Kutta method.

2.3. *Grid resolution tests and flow features*

To ensure that the grid resolution used is sufficient for the present direct numerical simulation, we examine the Kolmogorov length scale in the turbulent mixing zone, which is calculated by

$$\eta = \frac{1}{\sqrt{Re}} \frac{1}{\sqrt{\langle \rho \rangle}} \left(\frac{\langle \mu \rangle^3}{\langle \varepsilon \rangle} \right)^{1/4}, \qquad (2.8)$$

where ε is the viscous dissipation rate and $\langle f \rangle = (L_x L_y h)^{-1} \int_{h_S}^{h_B} \iint f \, dx \, dy \, dz$ denotes the volume average in the mixing region. Here, h means the entrainment width of mixing region, where the entrained fluids are perfectly homogenized in the horizontal plane (Cabot & Cook 2006), and is the sum of the mean thicknesses of bubbles and spikes (Gauthier 2017), i.e. h_B and h_S:

$$h_S = \int_{-L_z/2}^{0} M(\bar{T}) \, dz \quad \text{and} \quad h_B = \int_{0}^{L_z/2} M(\bar{T}) \, dz. \qquad (2.9a,b)$$

Here, a mixing function $M(T) = 4(T - T_{up})(T_{low} - T)/(T_{low} - T_{up})^2$ is employed with $0 \leq M \leq 1$ (Dalziel, Linden & Youngs 1999; Vladimirova & Chertkov 2009) and the overbar denotes the spatial average in the horizontal plane.

To ensure the reliable prediction of statistics by means of direct numerical simulation, as indicated by Yeung & Pope (1989), a resolution criterion of $k_{max}\eta \geq 1$ is adequate for low-order velocity statistics, while a criterion of $k_{max}\eta \geq 1.5$ is required for higher-order statistics (such as dissipation rate statistics), where k_{max} stands for the maximum wavenumber resolved. As shown in figure 1(*a*), the normalized Kolmogorov length scale $k_{max}\eta$ decreases gradually for $t/\tau < 1.5$ and approaches a plateau value ~ 3 when $t/\tau > 2$, where $\tau = (L_z Fr/At)^{1/2}$ is the characteristic time of the RT flow (Kord & Capecelatro 2019). This behaviour is well captured for the evolution of RTI from the early stage to turbulent mixing. Furthermore, it is identified that $\eta/\Delta \simeq 1.0$ at $t/\tau = 3.0$, where Δ is the grid width used in this study. Thus the present grid resolution can reliably predict the compressible RT flow and is enough to properly capture the smallest scales of the flow.

Moreover, the evolution of RT flow can be measured in terms of the so-called outer scale Reynolds number defined as $Re_H = \rho_I H \dot{H}/\mu_I$ (Cook & Zhou 2002; Cabot & Cook 2006), where H is the visual width of mixing region defined as the mean vertical range with the mixing function $M(\bar{T}) > 0.01$. Here $H = 2.1h$ has been used to ensure $M(\bar{T}) > 0.01$ in the mixing region. Usually a critical Re_H value $\sim 10^4$ is required for a mixing transition to fully developed turbulence (Dimotakis 2000). It is seen from figure 1(*b*) that Re_H has a significant increase to the order of $\sim 10^4$ at $t/\tau \approx 2$, and then up to 2.6×10^4 at $t/\tau = 3.0$. It is identified that the Reynolds number grows with a t^3 scaling for $t/\tau > 2$ approximately, which means a fully developed state is achieved in the mixing region of the RT flow (Cook & Zhou 2002).

Further, the kinetic energy spectra are employed to determine that the grid resolution used is fine enough. Figure 2(*a*) shows the kinetic energy spectra $E(k)$ calculated in the horizontal plane at $z = 0$ at $t/\tau = 1.0$, 2.0 and 3.0. Two typical features are demonstrated obviously in the spectra $E(k)$ versus time: an increase of peak value up to several orders
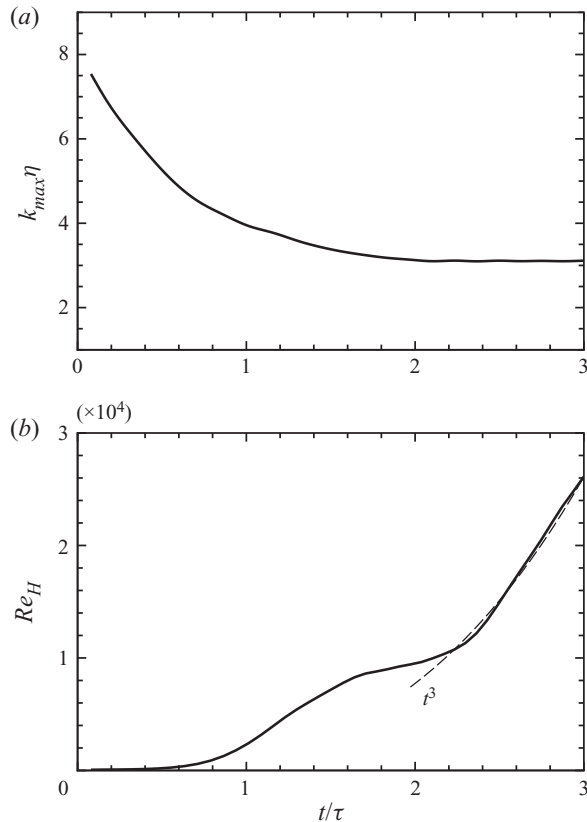
FIGURE 1. Evolution of the mean normalized Kolmogorov length scale (*a*) and outer scale Reynolds number (*b*).

shifting towards low wavenumbers and an occurrence of an inertial range as evidenced by the well-fitted power law. The former feature indicates an increasing dominance of larger-scale structures that are formed due to the merging of bubbles and spikes. This is facilitated by the continuous energy injection as the buoyancy converts energy from potential to kinetic energy. The latter implies that a fully developed state of turbulent mixing is realized at approximately $t/\tau = 2.0$. Note that the spectra obtained are consistent with a power law of $-7/4$ for the inertial range predicted by Zhou (2001), different from the classical Kolmogorov law, i.e. $-5/3$. This feature is reasonably related to the external time scale introduced by the buoyancy (Cook & Zhou 2002). Further, figure 2(*b*) shows the velocity spectra $E_u(k)$, $E_v(k)$ and $E_w(k)$ at $t/\tau = 3.0$. The velocity spectra exhibit stronger anisotropy at large scales than at small scales. In particular, $E_w(k)$ is higher by about one order of magnitude than $E_u(k)$ and $E_v(k)$ at large scales.

The flow structures are well captured for RT turbulence under the present grid resolution. Figure 3 typically shows a snapshot of the instantaneous temperature field at $t/\tau = 3.0$. It exhibits fine-scale structures and large patches of mixed fluids. Specifically, large-scale structures are well identified in the turbulent mixing zone, which arise as the merging of bubbles and spikes. Small-scale structures are also fully resolved along the evolutional interface between the hot (ascending) and cold (descending) fluids.
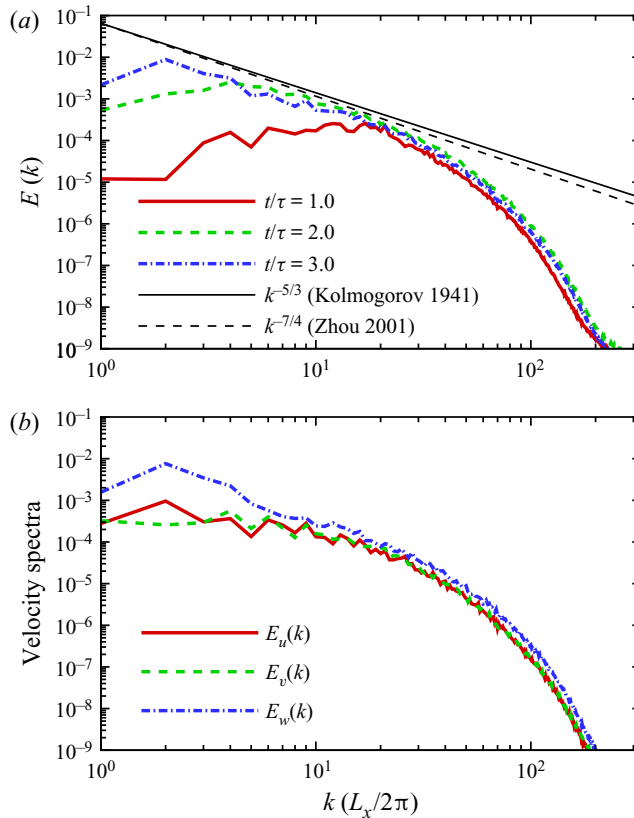
FIGURE 2. Kinetic energy spectra $E(k)$ (*a*) at instants $t/\tau = 1.0$, 2.0 and 3.0 and velocity spectra (*b*) at $t/\tau = 3.0$ in the horizontal plane at $z = 0$. Here, the horizontal wavenumber $k = \sqrt{k_x^2 + k_y^2}$.

This visualization indicates clearly the non-stationary and non-isotropic feature of compressible RT turbulence (Boffetta *et al.* 2009).

In addition, we have carefully examined the physical model and numerical approach used in this study and have verified that the calculated results are reliable in our previous work on compressible turbulent boundary layer (Wang & Lu 2012; Chu & Lu 2013) and on compressible turbulent mixing layer (Yu & Lu 2019, 2020).

3. Generation and transfer of kinetic energy

3.1. *Generation of kinetic energy*

Energy conversion from potential to kinetic energy is first investigated in compressible RT flows by means of the kinetic energy budget. From the momentum equation (2.2) the transport equation of kinetic energy is derived as

$$\frac{\partial}{\partial t}\left(\frac{1}{2}\rho u_i u_i\right) + \frac{\partial}{\partial x_j}\left(\frac{1}{2}\rho u_i u_i u_j + p u_j - \frac{1}{Re}u_i\tau_{ij}\right) = p\theta - \frac{1}{Re}\tau_{ij}\frac{\partial u_i}{\partial x_j} - \frac{1}{Fr}\rho u_3. \quad (3.1)$$
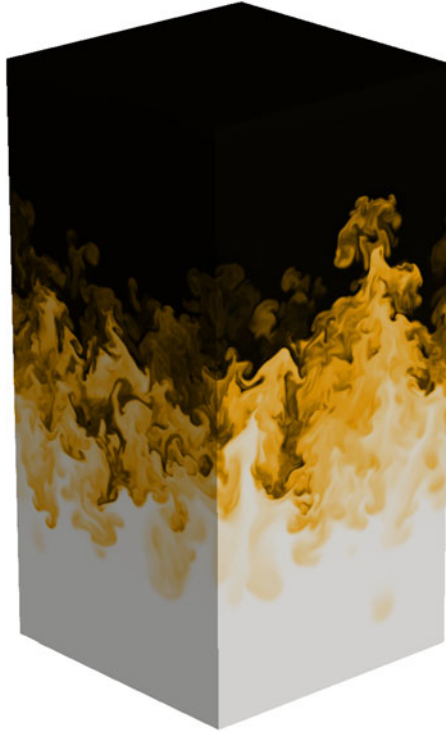
FIGURE 3. Snapshot of instantaneous temperature field for compressible RT turbulence at $t/\tau = 3.0$. Here, white and black colour regions represent the hot and cold fluids, respectively.

By integrating equation (3.1) over the flow domain, we have the global kinetic energy budget

$$-\frac{\mathrm{d}P}{\mathrm{d}t} + W = \frac{\mathrm{d}K}{\mathrm{d}t} + \varepsilon, \tag{3.2}$$

where $P = (1/Fr)\int_V \rho z\, \mathrm{d}V$ is the potential energy, $K = \int_V \frac{1}{2}\rho u_i u_i\, \mathrm{d}V$ is the kinetic energy, $\varepsilon = (1/Re)\int_V \tau_{ij}(\partial u_i/\partial x_j)\, \mathrm{d}V$ is the energy dissipation rate and $W = \int_V p\theta\, \mathrm{d}V = \int_V p(\partial u_k/\partial x_k)\, \mathrm{d}V$ is the pressure-dilatation power term. Note that the pressure-dilatation power term is related to the power of pressure work due to the compressing process in compressible RT flows, which plays an important role in the local conversion between kinetic energy and internal energy (Wang *et al.* 2018). A positive W means that the dilatation effect contributes to the generation of kinetic energy, and vice versa. Moreover, the other terms integrated in (3.1) vanish because the periodic and flux-free conditions are applied in the horizontal and vertical boundaries, respectively.

Based on (3.2), it is identified that there exist two mechanisms for the generation of kinetic energy, namely the conversion of potential energy to kinetic energy and the pressure work related to the compressibility of fluid elements. Thus, the two mechanisms are first investigated based on the budget terms of (3.2). As shown in figure 4, $\mathrm{d}K/\mathrm{d}t$ remains positive during flow evolution, which means a continuous increase of the kinetic energy. This behaviour is associated with two factors as indicated in (3.2). The term $\mathrm{d}P/\mathrm{d}t$ is a negative distribution, which means the persisting conversion of potential energy into kinetic energy. In reality, the conversion acts as a major mechanism for the generation of
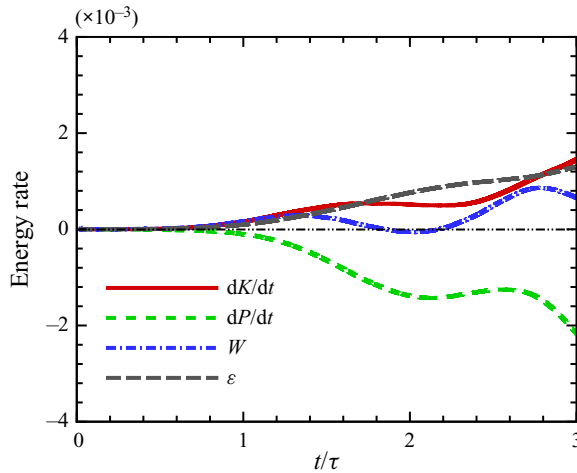
FIGURE 4. Evolution of the budget terms of kinetic energy in (3.2).

kinetic energy as evidently shown for $t/\tau > 1$. Rather than trivial as in incompressible RT flows (Cabot & Cook 2006; Zhou 2013), the pressure-dilatation power W is comparable to $\mathrm{d}K/\mathrm{d}t$, especially at $t/\tau \approx 1.2$ and 2.8 where two peaks occur obviously. The evolution of W reveals that the dilatation effects serve as an important source to generate kinetic energy in the development of RT turbulence. Moreover, ε increases with flow evolution to account for the kinetic energy dissipation.

The overall energy balance can be quantified by taking a temporal integration of (3.2) from 0 to t, which gives

$$- \delta P(t) + \delta W(t) = \delta K(t) + \Psi(t), \tag{3.3}$$

where $-\delta P(t)$ is the total potential energy, $\delta W(t)$ is the total pressure-dilatation work related to the overall dilatation effect, $\delta K(t)$ is the total kinetic energy increase of the RT system considered and $\Psi(t)$ is the total energy dissipation. It is identified from (3.3) that the total input energy for the RT system is responsible for the total production, i.e. $-\delta P + \delta W$. Therefore, the overall production efficiency of kinetic energy can be evaluated by the ratio $\delta K/(-\delta P + \delta W)$ and the overall dilatation effect on the generation of kinetic energy by the ratio $\delta W/(-\delta P + \delta W)$.

Figure 5 shows the two ratios during the evolution of compressible RT flow. The overall production efficiency $\delta K/(-\delta P + \delta W)$ increases gradually from 20 % in the early stage and reaches a level of over 50 %. Then it decreases slightly to around 45 % in the later stage. When the ratio $\delta W/(-\delta P + \delta W)$ is around 1, it means that the dilatation effect is almost fully responsible for the generation of kinetic energy. This behaviour is related to the non-uniform initial temperature induced by a non-zero time derivative in energy equation (2.3), i.e. $\partial_t(\rho e) = (1/RePr)\partial_j(\partial_j T)$. For the compressible RT flow considered here, the dilatational velocity can be demonstrated by the contour patterns of dilatation as shown in figure 6. It is seen that the dilatation patterns of $\theta > 0$ appear in the regions with relatively higher pressure and vice versa, accounting for the prevailing contribution of $\delta W(t)$ to the generation of kinetic energy. The overall dilatation effect remains prevalent over the conversion of potential energy for $t/\tau < 1.5$ approximately as the ratio $\delta W/(-\delta P + \delta W) > 0.5$. Then this situation changes for $t/\tau > 1.5$ as $\delta W/(-\delta P + \delta W) < 0.5$. In turbulent mixing, this ratio reaches 0.1–0.2, indicating
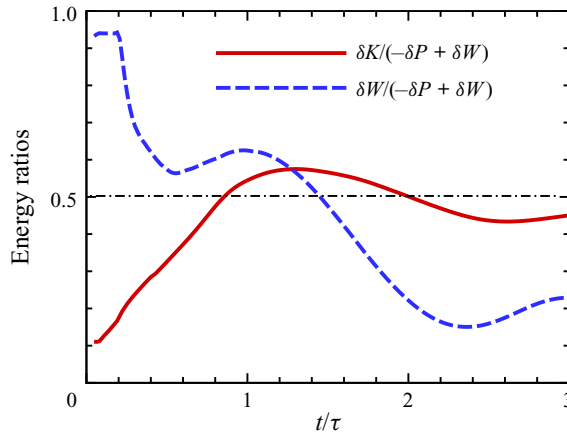
FIGURE 5. Ratios of the total kinetic energy change to total production and of the pressure-dilatation work to total production.
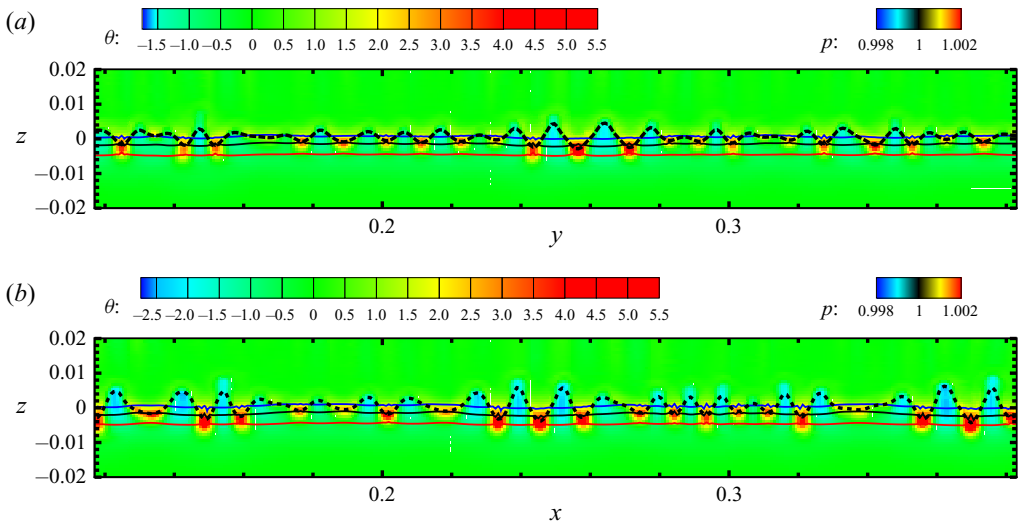

FIGURE 6. Contour plots of dilatation (coloured pattern) and pressure (coloured line) near the interface at $t/\tau = 0.16$ in (*a*) the y–z plane at $x = 0.25$ and (*b*) the x–z plane at $y = 0.25$.

that the conversion of potential energy offers the main contribution to the kinetic energy rather than the pressure-dilatation work.

In order to clarify the effect of kinetic energy generation mechanisms on compressible RT turbulence, we investigate the scaling exponents of longitudinal velocity structures by means of the approaches used for two-dimensional incompressible RT turbulence (e.g. Celani, Mazzino & Vozella 2006) and for three-dimensional incompressible RT turbulence (e.g. Matsumoto 2009). Figure 7(*a*) shows the temporal scaling of the velocity structure functions at spatial scale $x/L_x = 0.1$, which is chosen based on the fact that this spatial scale lies in the inertial range from the kinetic energy spectra in figure 2(*a*). It is identified that there exist two scaling expone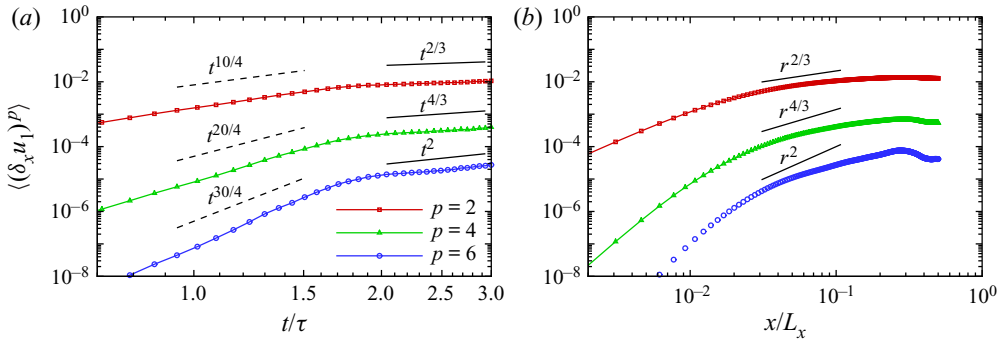nts for two typical stages of developing state for $t/\tau < 1.5$ approximately and fully developed state for $t/\tau > 2.0$

FIGURE 7. Longitudinal velocity structures $\langle (\delta_x u_1)^p \rangle$ along the x direction, where u_1 is the x component of the velocity, as functions of (*a*) time t/τ at spatial scale $x/L_x = 0.1$ and (*b*) distance x/L_x at time $t/\tau = 3.0$. Solid lines represent the phenomenological predictions by Chertkov (2003). Dashed lines represent the fitted curve slopes.

of turbulent mixing. According to the results shown in figure 5, the reason is possibly associated with different mechanisms of kinetic energy generation in the two stages. The pressure-dilatation work dominates the generation of kinetic energy for $t/\tau < 1.5$, while the potential energy conversion provides the main contribution for $t/\tau > 2.0$. Hence, the scaling exponents in the fully developed state ($t/\tau > 2.0$) in figure 7(*a*) agree quite well with the phenomenological predictions (Chertkov 2003), i.e. $\delta_r u \sim (Atg)^{2/3} r^{1/3} t^{1/3}$, for incompressible RT turbulence at the fully developed stage in which the potential energy conversion dominates the generation of kinetic energy.

Figure 7(*b*) also shows the spatial scaling of the velocity structure functions at time $t/\tau = 3.0$ when a fully developed state is achieved in the mixing region of RT flow. It is seen that the scaling exponents of the second-order velocity structure functions are approximately consistent with the phenomenological predictions (Chertkov 2003). However, the scaling exponents of the higher-order velocity structure functions no longer agree with the phenomenological predictions (Chertkov 2003). Such obvious deviations were also reported by Matsumoto (2009) for three-dimensional incompressible turbulence. The possible reason for these obvious deviations may be related to the anisotropic behaviour in RT turbulence and the narrow inertial range at relatively low Reynolds number.

3.2. *Transfer of kinetic energy*

The scale-to-scale transfer of kinetic energy is investigated for compressible RT turbulence. The relevant problem has never been discussed before. Here we apply a recently developed filtering approach (Aluie 2011, 2013; Wang *et al.* 2013) to analyse the kinetic energy transfer. A filter operator is represented as

$$\bar{f}_r(\boldsymbol{x}) = \int G_r(\boldsymbol{x}') f(\boldsymbol{x} + \boldsymbol{x}') \, \mathrm{d}\boldsymbol{x}', \tag{3.4}$$

where G_r is a Gaussian filter and the subscript r denotes a function f containing the information only at length scales larger than r. For the present compressible RT turbulence, the Favre filter is also used and defined as $\tilde{f} = \overline{\rho f}/\bar{\rho}$. Then a large-scale kinetic energy equation (Aluie 2011, 2013; Wang *et al.* 2013) can be given as

$$\frac{\partial}{\partial t} \left(\frac{\bar{\rho}_r |\tilde{\boldsymbol{u}}_r|^2}{2} \right) + \nabla \cdot \boldsymbol{J}_r = -\Pi_r - \Lambda_r + \Phi_r - \varepsilon_r + I_r, \tag{3.5}$$

where $\frac{1}{2}\bar{\rho}_r|\tilde{\boldsymbol{u}}_r|^2$ is the large-scale kinetic energy and the other terms are defined as

$$(\boldsymbol{J}_r)_j = \bar{\rho}\frac{|\tilde{\boldsymbol{u}}_r|^2}{2}\tilde{u}_j + \overline{pu}_j + \tilde{u}_i\bar{\rho}\left(\widetilde{u_iu_j} - \tilde{u}_i\tilde{u}_j\right) - \frac{1}{Re}\tilde{u}_i\bar{\tau}_{ij}, \tag{3.6a}$$

$$\Pi_r = -\bar{\rho}\left(\widetilde{u_iu_j} - \tilde{u}_i\tilde{u}_j\right)\frac{\partial\tilde{u}_i}{\partial x_j}, \tag{3.6b}$$

$$\Lambda_r = \frac{1}{\bar{\rho}}\frac{\partial\bar{p}}{\partial x_j}\left(\overline{\rho u_j} - \bar{\rho}\,\bar{u}_j\right), \tag{3.6c}$$

$$\Phi_r = \bar{p}\frac{\partial\bar{u}_i}{\partial x_i}, \tag{3.6d}$$

$$\varepsilon_r = \frac{1}{Re}\bar{\tau}_{ij}\frac{\partial\tilde{u}_i}{\partial x_j}, \tag{3.6e}$$

$$I_r = -\frac{1}{Fr}\bar{\rho}\tilde{u}_3. \tag{3.6f}$$

Here, $\boldsymbol{J}_r$ is the spatial transport of the large-scale kinetic energy; Π_r is the deformation work done by large-scale strain $\partial\tilde{u}_i/\partial x_j$ against the subgrid stress $\bar{\rho}(\widetilde{u_iu_j} - \tilde{u}_i\tilde{u}_j)$, which represents the kinetic energy transfer from the filtered scale to smaller scale; Λ_r is the baropycnal work done by the large-scale pressure gradient $(1/\bar{\rho})(\partial\bar{p}/\partial x_j)$ against the subscale mass flux $\overline{\rho u_j} - \bar{\rho}\,\bar{u}_j$ (Aluie 2011, 2013), which also means the kinetic energy transfer to scales smaller than r; Φ_r is the large-scale pressure dilatation related to the flow compressibility; ε_r is the large-scale viscous dissipation term; and I_r is the energy injected by gravity.

Figure 8 shows the terms on the right-hand side of (3.5) averaged in the mixing region versus the normalized filter scale r/η at several instants $t/\tau = 1.0$, 2.0 and 3.0. It is seen that the kinetic energy is generated by the pressure dilatation Φ_r and the injection of gravity I_r at all scales. The pressure dilatation is larger than the injection of gravity at $t/\tau = 1.0$, then becomes less than the injection of gravity at $t/\tau = 2.0$ and 3.0, which differs from Boussinesq RT turbulence where kinetic energy is only generated by gravity at all scales (Chertkov 2003; Zhou *et al.* 2016). This behaviour indicates that the compressibility plays as an important role in the generation of kinetic energy at all scales. The kinetic energy is dissipated by the viscous effect and the viscous dissipation becomes stronger at smaller scales. Furthermore, the characteristics of the deformation work and the baropycnal work are worthy of concern. The deformation work is negative in the large filter scales at $t/\tau = 1.0$, then becomes positive at $t/\tau = 2.0$ and 3.0, since the formation of large-scale structures caused by the merger of bubbles and spikes allows the kinetic energy transfer from large to small scales. Then the peak of deformation work is gradually formed at the filter scale $r/\eta \approx 50$ with the flow evolution. The baropycnal work is always positive in all scales, indicating that the kinetic energy is transferred from large to small scales under its action and the kinetic energy transfer becomes stronger with an increase of the scale. Based on the investigation of Lees & Aluie (2019) in compressible isotropic homogeneous turbulence (IHT), the baropycnal work occurs only in variable density flows. This is well consistent with the physical mechanisms of compressible IHT that the baropycnal work arises in RT turbulence which is a canonical variable
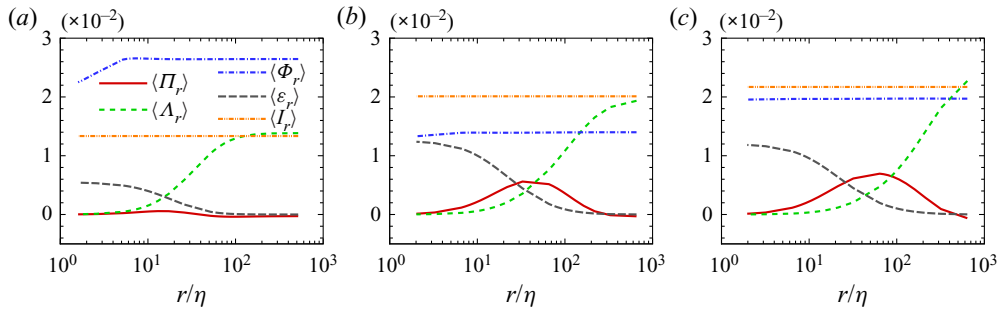
FIGURE 8. The average terms of the large-scale kinetic energy equation versus the normalized filter scale r/η at different instants: (a) $t/\tau = 1.0$, (b) $t/\tau = 2.0$ and (c) $t/\tau = 3.0$.

density flow. However, different from compressible RT turbulence, the baropycnal work in compressible IHT is negative (Wang *et al.* 2013; Lees & Aluie 2019) and the total amount of energy transfer across scales is effectively reduced. Moreover, the pressure and density gradients in compressible IHT have the same direction to align with the contracting strain eigenvector across a shock, leading to negative baropycnal work (Lees & Aluie 2019). In the mixing region of RT turbulence, the pressure and density gradients have the opposite direction, resulting in positive baropycnal work. By comparing the deformation work with the baropycnal work, it is found that the deformation work is greater than the baropycnal work in small filter scales, while it becomes less than the baropycnal work in large filter scales.

Further we investigate the deformation work and the baropycnal work at three filter scales $r/\eta = 10$, 50 and 100, as shown in figure 9. It is seen that a peak of the baropycnal work occurs and increases with an increase of filter scale. The deformation work is strengthened gradually over time and becomes stabilized approximately for RT turbulence. Meanwhile a negative value in the early stage of flow evolution occurs at $r/\eta = 50$ and 100 because the large-scale structure has not formed yet. The deformation work becomes greater than the baropycnal work at $r/\eta = 10$ and 50 at the late stage. It is also noticed that the baropycnal work is always greater than the deformation work at $r/\eta = 100$. The underlying mechanisms can be analysed as follows. Both the deformation work and the baropycnal work reflect that the kinetic energy is transferred from large to small scales. The deformation work plays a major role in scale-to-scale kinetic energy transfer in the small-scale regime, while the baropycnal work plays a major role in scale-to-scale kinetic energy transfer in the large-scale region for RT turbulence.

As mentioned above, a peak of the baropycnal work occurs. The baropycnal work is done by the large-scale pressure gradient against the subscale mass flux. Therefore, when the entrainment width of the mixing region equals the filter scale, the baropycnal work will achieve the maximum value as the appearance of more subscale mass flux in the mixing region. To verify the above analysis, a characteristic time t^* when $h = r$ is defined. Figure 10(a) shows the normalized entrainment width of mixing region h/η versus time. Three characteristic times $t_1^* = 0.55$, 1.01 and 1.29 are determined for the filter scales $r/\eta = 10$, 50 and 100, respectively. Further, the baropycnal work at three filter scales $r/\eta = 10$, 50 and 100 versus the renormalized time t/t^* is shown in figure 10(b). It is seen that the peaks of baropycnal work at different filter scales occur at the corresponding characteristic times approximately.
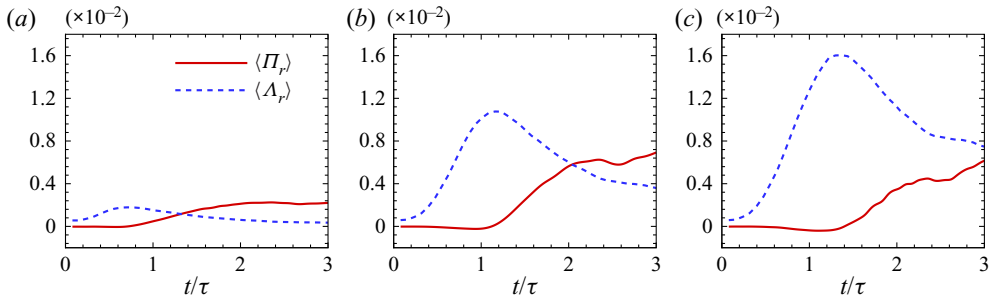
FIGURE 9. The average deformation work and baropycnal work versus time at different filter scales: (*a*) $r/\eta = 10$, (*b*) $r/\eta = 50$ and (*c*) $r/\eta = 100$.
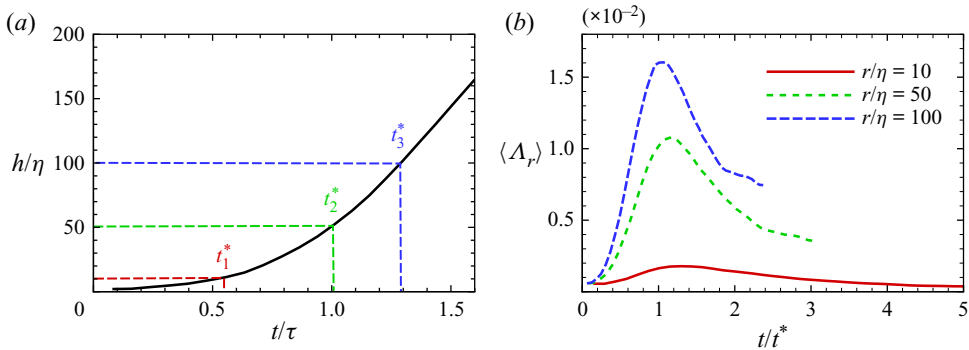

FIGURE 10. (*a*) The normalized entrainment width of mixing region h/η versus time. (*b*) The average baropycnal work versus the renormalized time at three different filter scales.

3.3. *Effect of compressibility on baropycnal work*

The baropycnal work is the work done by large-scale pressure gradient against the subscale mass flux, which is intrinsically due to the compressibility effect and vanishes in the absence of density variations (Aluie 2013). To reveal the relationship between the baropycnal work and compressibility, we decompose the baropycnal work Λ_r into a positive component Λ_r^+ and a negative component Λ_r^-, which are defined as

$$\Lambda_r^+ = \tfrac{1}{2}(\Lambda_r + |\Lambda_r|), \quad \Lambda_r^- = \tfrac{1}{2}(\Lambda_r - |\Lambda_r|). \tag{3.7a,b}$$

Figure 11 shows the positive and negative components of baropycnal work averaged in the mixing region as a function of the normalized filter scale r/η at $t/\tau = 1.0$, 2.0 and 3.0. It is found that the positive component acts a major contribution to the baropycnal work. The behaviour indicates that the kinetic energy transfer caused by the baropycnal work is mainly transferred from large to small scales. As a vertically downward large-scale pressure gradient occurs in the flow field under the action of gravity, the downward movement of the small-scale spike structures makes the baropycnal work positive, and the upward movement of the small-scale bubble structures makes the baropycnal work negative. Since the density of the spike structures is large and the density of the bubble structures is small, the baropycnal work is positive and the kinetic energy is transferred from large to small scales. The larger the filter scale, the greater is the positive component
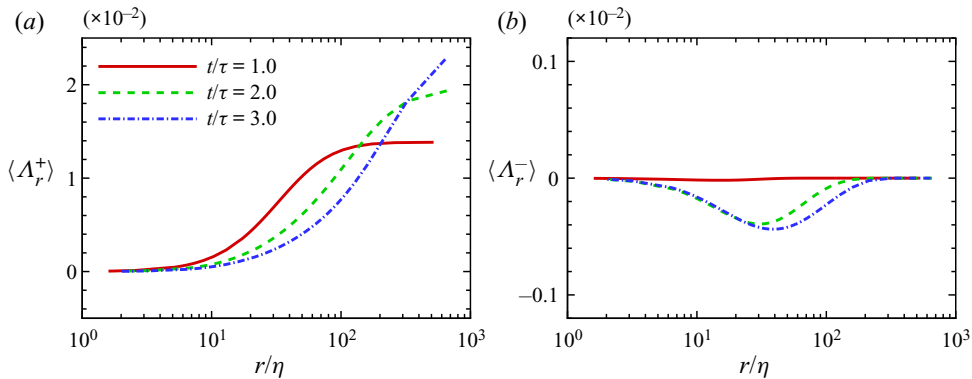
FIGURE 11. The positive and negative components of baropycnal work versus the normalized filter scale r/η for different instants: (*a*) positive components; (*b*) negative components.
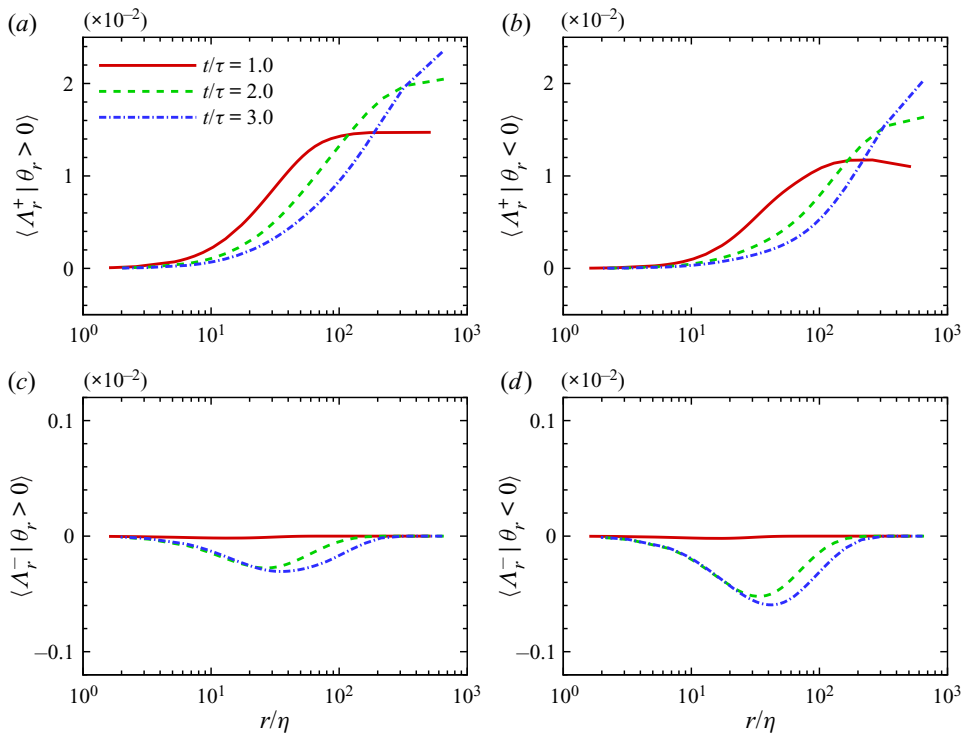

FIGURE 12. Conditional average of the positive and negative components of baropycnal work versus the normalized filter scale r/η for different instants.

of baropycnal work, because it contains more small-scale bubble and spike structures at the larger filter scales.

In order to deal with the effect of compressibility on the baropycnal work, we consider the following conditional average of the positive and negative components of baropycnal work, i.e. $\langle \Lambda_r^+ \mid \theta_r > 0 \rangle$, $\langle \Lambda_r^+ \mid \theta_r < 0 \rangle$, $\langle \Lambda_r^- \mid \theta_r > 0 \rangle$ and $\langle \Lambda_r^- \mid \theta_r < 0 \rangle$, where θ_r is the filtered velocity divergence. Figure 12 shows the conditional average of the positive and
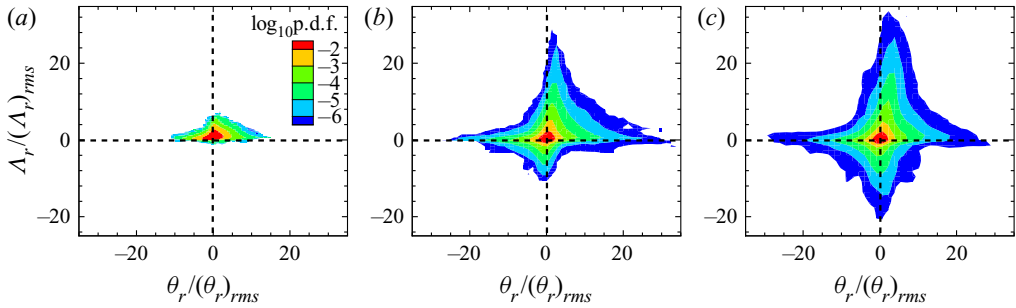
FIGURE 13. Joint p.d.f. of $\Lambda_r/(\Lambda_r)_{rms}$ and $\theta_r/(\theta_r)_{rms}$ for the filter scale $r/\eta = 50$ at different instants: (*a*) $t/\tau = 1.0$, (*b*) $t/\tau = 2.0$ and (*c*) $t/\tau = 3.0$.

negative components of baropycnal work versus the normalized filter scale r/η at $t/\tau = 1.0$, 2.0 and 3.0. For the conditional average of the positive component, the conditional average for $\theta_r > 0$ is greater than that for $\theta_r < 0$. However, for the conditional average of the negative component, the conditional average for $\theta_r > 0$ is less than that for $\theta_r < 0$. Therefore, the expansion motion ($\theta_r > 0$) enhances the positive baropycnal work so that the kinetic energy is transferred from large to small scales, while the compression motion ($\theta_r < 0$) strengthens the negative baropycnal work so that the kinetic energy is transferred from small to large scales.

To further illustrate the relationship between the baropycnal work and compressibility, figure 13 shows the joint probability density function (p.d.f.) of the normalized baropycnal work $\Lambda_r/(\Lambda_r)_{rms}$ and the velocity divergence $\theta_r/(\theta_r)_{rms}$ for the filter scale $r/\eta = 50$ at $t/\tau = 1.0$, 2.0 and 3.0. At $t/\tau = 1.0$, the shape of the joint p.d.f. is approximately symmetric with respect to $\theta_r/(\theta_r)_{rms} = 0$. At $t/\tau = 2.0$ and 3.0, the shape of the joint p.d.f. is asymmetric with the larger probability in the first and third quadrants. This means that the expansion regions provide a major contribution to the positive component of the baropycnal work and the compression regions to the negative component of the baropycnal work. Because of the compressibility effect, the expansion motion enhances the positive baropycnal work so that the kinetic energy is transferred from large to small scales, and the compression motion strengthens the negative baropycnal work so that the kinetic energy is transferred from small to large scales. Since a vertical downward pressure gradient occurs, the large-density spike structures move downward and the small-density bubble structures move upward, resulting in the baropycnal work being mainly positive.

4. Generation and transfer of enstrophy

4.1. *Generation of enstrophy*

In compressible RT turbulence, the enstrophy, defined as $\Omega = \frac{1}{2}\omega_i\omega_i$ with the vorticity component ω_i, is usually generated by the baroclinic effect and its anisotropy is formed by the gravity effect. The underlying mechanisms of the generation and evolution of enstrophy are desirable to be studied. Here the enstrophy transport equation is employed for the present study and is given as

$$\frac{d}{dt}\left(\frac{1}{2}\omega_i\omega_i\right) = P_\omega + D_\omega + B_\omega + V_\omega, \tag{4.1}$$
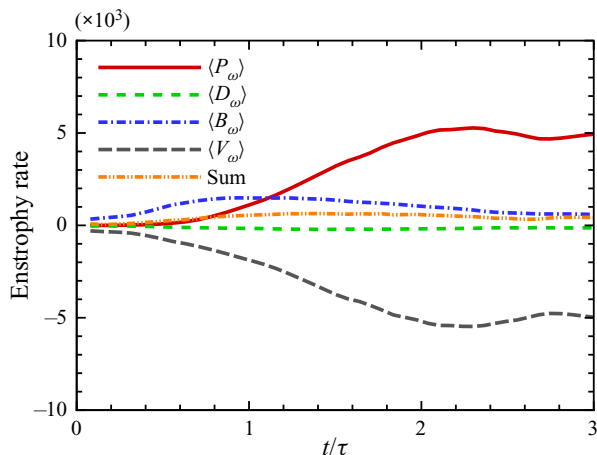
FIGURE 14. The average terms of the enstrophy transport equation versus time. Here, $\langle P_\omega \rangle$ is the vortex stretching and tilting term, $\langle D_\omega \rangle$ is the dilatation term, $\langle B_\omega \rangle$ is the baroclinic term, $\langle V_\omega \rangle$ is the viscous term and Sum denotes the sum of these four terms.

where $P_\omega = \omega_i S_{ij} \omega_j$ is the vortex stretching and tilting term with the strain rate tensor $S_{ij} = \frac{1}{2}(\partial u_i / \partial x_j + \partial u_j / \partial x_i)$, $D_\omega = -\omega_i \omega_i (\partial u_k / \partial x_k)$ is the dilatation term related to the compressibility effect, $B_\omega = (1/\rho^2) \varepsilon_{ijk} \omega_i (\partial \rho / \partial x_j)(\partial p / \partial x_k)$ is the baroclinic term with the alternating tensor ε_{ijk}, and $V_\omega = (1/Re) \varepsilon_{ijk} \omega_i (\partial / \partial x_j)((1/\rho)(\partial \tau_{lk}/\partial x_l))$ is the viscous term.

Figure 14 shows the terms on the right-hand side of (4.1) averaged in the mixing region. It is identified that the sum of the four terms is always positive, indicating that the enstrophy increases during flow evolution. Furthermore, the baroclinic term is larger than the vortex stretching and tilting term before $t/\tau = 1.2$ and becomes small after $t/\tau = 2.0$. Thus the enstrophy is generated by the baroclinic effect at the early stage of flow evolution and is enhanced by vortex stretching and tilting at the late stage. However, the vortex stretching and tilting term, which is the mechanism acting to transfer large-scale energy and enstrophy to small scales, disappears in two-dimensional flow (Cabot 2006). Hence, two- and three-dimensional systems would have a totally different phenomenology in compressible RT turbulence. The viscous term is always negative for the dissipation of enstrophy. Compressibility has a little effect on the enstrophy because the dilatation term is small.

To discuss the anisotropy of RTI-induced flows, the vertical and horizontal enstrophy transport equations are used to analyse the enstrophy in different directions. The vertical enstrophy transport equation is

$$\frac{d}{dt}\left(\frac{1}{2}\omega_3\omega_3\right) = \omega_3 S_{3j}\omega_j - \omega_3\omega_3\frac{\partial u_k}{\partial x_k} + \frac{\omega_3}{\rho^2}\varepsilon_{3jk}\frac{\partial \rho}{\partial x_j}\frac{\partial p}{\partial x_k} + \frac{1}{Re}\varepsilon_{3jk}\omega_3\frac{\partial}{\partial x_j}\left(\frac{1}{\rho}\frac{\partial \tau_{lk}}{\partial x_l}\right). \quad (4.2)$$

Moreover, the horizontal enstrophy transport equation can be obtained by subtracting (4.2) from (4.1).

Figure 15 shows the terms of the vertical and horizontal enstrophy transport equations. The horizontal and vertical enstrophy is dissipated by the viscous effect and the compressibility has little effect on the enstrophy. The horizontal enstrophy is generated by the baroclinic effect in the early stage of flow evolution and is enhanced by vortex stretching and tilting in turbulent mixing. On the other hand, the vertical enstrophy is
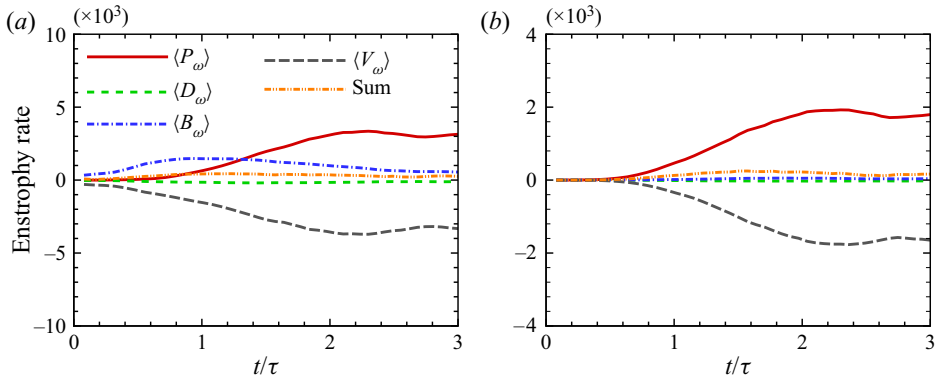
FIGURE 15. The average terms of the vertical and horizontal enstrophy transport equation versus time: (*a*) horizontal enstrophy transport equation; (*b*) vertical enstrophy transport equation. For a description of the terms, see the caption to figure 14.
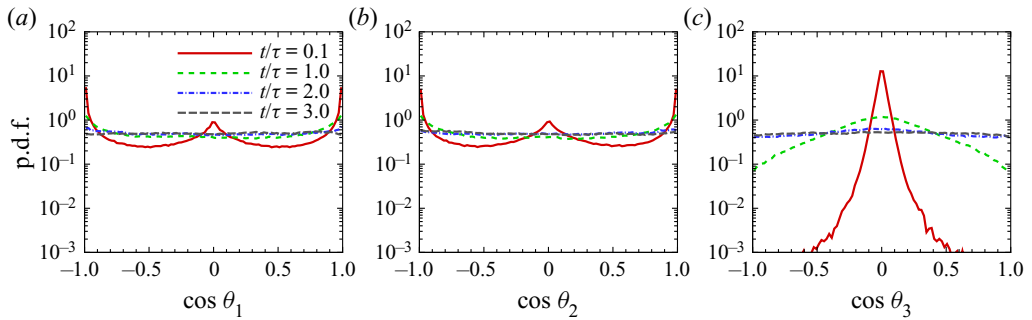

FIGURE 16. The p.d.f. of vorticity direction cosine at several instants: (*a*) *x*-direction cosine, (*b*) *y*-direction cosine and (*c*) *z*-direction cosine.

mainly generated by vortex stretching and tilting and the baroclinic effect is weak. It is noticed that the vertical baroclinic effect no longer vanishes in compressible RT turbulence which differs from Boussinesq RT turbulence (Schneider & Gauthier 2016). Thus the horizontal enstrophy is mainly generated by the baroclinic effect and the vertical enstrophy by vortex stretching and tilting during flow evolution.

To further illustrate the evolution of vorticity in different directions, figure 16 shows the p.d.f.s of the vorticity direction cosine, where the vorticity direction cosine is defined as

$$\cos \theta_i = \frac{\omega_i}{\sqrt{\omega_1^2 + \omega_2^2 + \omega_3^2}}. \tag{4.3}$$

The vorticity direction is mainly the *x* and *y* directions at $t/\tau = 0.1$ and 1.0, because the vorticity is mainly generated by the baroclinic effect in the early stage of flow evolution. Then the vorticity tends to be eventually distributed in all three directions at $t/\tau = 2.0$ and 3.0, which is related to isotropic enstrophy formation by vortex stretching and tilting for RT turbulence.

4.2. *Transfer of enstrophy*

In order to investigate the scale-to-scale enstrophy transfer, we first derive the large-scale enstrophy equation in compressible flow. By means of the filter operation (3.4), the filtered large-scale enstrophy equation is given as

$$\frac{\partial \Omega_r}{\partial t} + \boldsymbol{\nabla} \cdot \boldsymbol{L}_r = -\Psi_r + P_r + D_r + B_r + V_r, \tag{4.4}$$

where $\Omega_r = \frac{1}{2}\bar{\omega}_i\bar{\omega}_i$ is the large-scale enstrophy and the other terms are defined as

$$(\boldsymbol{L}_r)_j = \Omega_r \bar{u}_j - \bar{\omega}_i \bar{Q}_{ij}, \tag{4.5a}$$

$$\Psi_r = \bar{Q}_{ij} \frac{\partial \bar{\omega}_i}{\partial x_j}, \tag{4.5b}$$

$$P_r = \bar{\omega}_i \bar{S}_{ij} \bar{\omega}_j, \tag{4.5c}$$

$$D_r = -\Omega_r \frac{\partial \bar{u}_k}{\partial x_k}, \tag{4.5d}$$

$$B_r = \varepsilon_{ijk}\bar{\omega}_i \overline{\frac{1}{\rho^2} \frac{\partial \rho}{\partial x_j} \frac{\partial p}{\partial x_k}}, \tag{4.5e}$$

$$V_r = \frac{1}{Re}\varepsilon_{ijk}\bar{\omega}_i \overline{\frac{\partial}{\partial x_j}\left(\frac{1}{\rho}\frac{\partial \tau_{lk}}{\partial x_l}\right)}, \tag{4.5f}$$

where $\bar{Q}_{ij} = \bar{q}_{ij} - \bar{q}_{ji}$ with $\bar{q}_{ij} = \overline{u_i \omega_j} - \bar{u}_i\bar{\omega}_j$; $\bar{S}_{ij} = \frac{1}{2}(\partial\bar{u}_i/\partial x_j + \partial\bar{u}_j/\partial x_i)$ is the large-scale strain rate tensor; $\boldsymbol{L}_r$ is the spatial transport of the large-scale enstrophy; Ψ_r is the scale-to-scale flux of the enstrophy, a positive value of Ψ_r denoting the enstrophy transfer from a scale larger than r to a scale smaller than r, and vice versa; P_r is the large-scale vortex stretching and tilting term; D_r is the large-scale vortex dilatation term related to the compressibility effect; B_r is the large-scale baroclinic term; and V_r is the large-scale viscous term.

Figure 17 shows the average terms on the right-hand side of (4.4) versus the normalized filter scale r/η at $t/\tau = 1.0, 2.0$ and 3.0. The scale-to-scale flux of enstrophy Ψ_r is positive, indicating that the enstrophy is transferred from large to small scales. It is interesting to notice that the enstrophy flux Ψ_r shows a peak at $r/\eta \simeq 10$, which approximately corresponds to cross-scale between the inertial range and the viscous range (Zhou 2013). The baroclinic effect B_r and the vortex stretching and tilting term P_r strengthen the generation of enstrophy as the filter scale decreases. Moreover, B_r is larger than P_r at $t/\tau = 1.0$, then it becomes less than P_r at $t/\tau = 2.0$ and 3.0. The vortex dilatation term D_r is almost zero, indicating that the compressibility has less effect on the generation of enstrophy at all scales. The viscous term V_r is always negative to dissipate the enstrophy, which also increases as the filter scale decreases.

Further, figure 18 shows the evolution of average terms of (4.4) at three typical filter scales $r/\eta = 10, 50$ and 100. The scale-to-scale flux of enstrophy Ψ_r gradually increases with time and tends to stabilize after $t/\tau = 2.0$ for fully turbulent mixing. Note that Ψ_r exhibits a negative distribution at $r/\eta = 100$ because the large-scale structure has not yet formed in the early stage. The baroclinic term B_r is larger than the vortex stretching and tilting term P_r and then it becomes less than P_r. The viscous term V_r is always negative for the three filter scales to dissipate the enstrophy by the viscous effect.
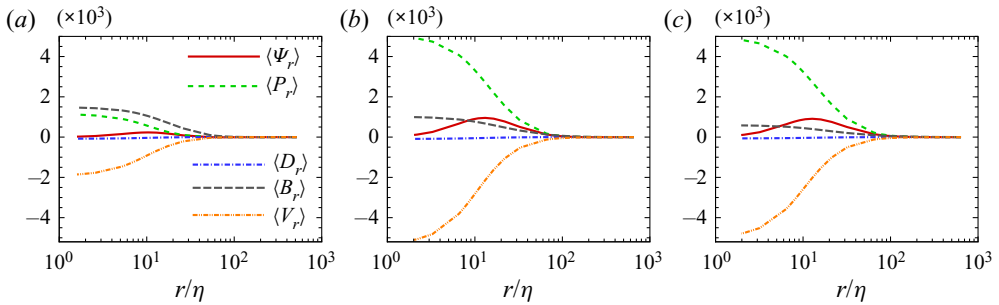
FIGURE 17. The average terms of the large-scale enstrophy equation as a function of the normalized filter scale r/η at different instants: (a) $t/\tau = 1.0$, (b) $t/\tau = 2.0$ and (c) $t/\tau = 3.0$.
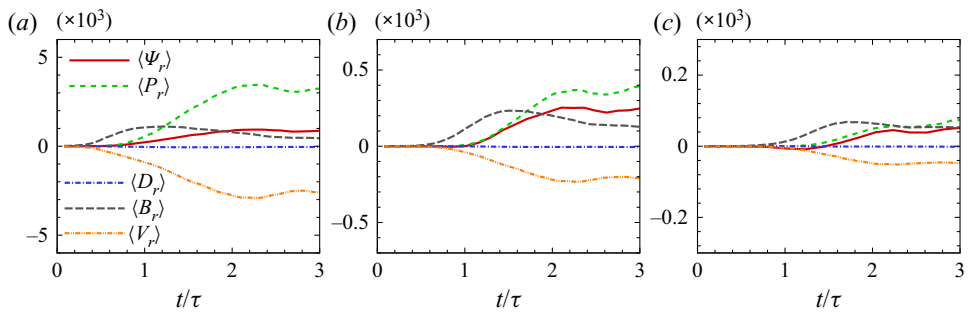

FIGURE 18. The average terms of the large-scale enstrophy equation versus time at different filter scales: (a) $r/\eta = 10$, (b) $r/\eta = 50$ and (c) $r/\eta = 100$.

5. Concluding remarks

The generation and transfer of kinetic energy and enstrophy in compressible RT turbulence were investigated by means of direct numerical simulation. The compressibility effects on the fundamental mechanisms dictating the RT turbulence behaviours were examined systematically and are summarized briefly as follows.

The generation of kinetic energy is investigated based on the kinetic energy budget equation. There are two mechanisms for the generation of kinetic energy in compressible RT turbulence. One is the conversion of potential energy to kinetic energy and the other is the pressure-dilatation work related to the compressibility of fluid elements. In addition to the persistence of conversion of potential energy into kinetic energy, the pressure dilatation also serves as an important source for generating kinetic energy at all scales during the development of RT turbulence. Moreover, there are two temporal scaling exponents of the velocity structure functions for the two stages of developing state and fully developed state of turbulent mixing under the effects of pressure-dilatation work and potential energy conversion. These behaviours indicate that compressibility plays an important role in the generation of kinetic energy of compressible RT flow.

The scale-to-scale transfer of kinetic energy is analysed for compressible RT turbulence by means of a large-scale kinetic energy equation. We identify two scale-to-scale fluxes of kinetic energy in compressible RT turbulence, i.e. the deformation work and baropycnal work. Positive deformation work and baropycnal work reflect that the kinetic energy is transferred from large to small scales on average for RT turbulence. The baropycnal work

is mainly responsible for the scale-to-scale kinetic energy transfer in large scales, and the deformation work for the kinetic energy transfer in small scales. Moreover, the baropycnal work is revealed to be related to the flow compressibility based on the finding that the expansion motion enhances the positive baropycnal work and the compression motion strengthens the negative baropycnal work. The relevant behaviours are also useful in the construction of turbulence models. Thus the compressibility not only affects the generation of kinetic energy, but also the transfer of kinetic energy in compressible RT turbulence.

The generation and scale-to-scale transfer of enstrophy are also studied based on transport and large-scale equations. The horizontal enstrophy is generated by the baroclinic effect and the vertical enstrophy by vortex stretching and tilting. Then the enstrophy is strengthened by vortex stretching and tilting during the evolution of RT flow and the vorticity tends to be isotropic in the turbulent mixing region. Further, the large-scale enstrophy equation in compressible flow is firstly derived to deal with the scale-to-scale transfer of enstrophy. It is revealed that at all scales the enstrophy is generated by the baroclinic effect in the early stage of flow evolution and is enhanced by vortex stretching and tilting in the late stage. The enstrophy is transferred from large to small scales on average and tends to stabilize for RT turbulence.

Acknowledgements

Declaration of interests

The authors report no conflict of interest.

REFERENCES

ALUIE, H. 2011 Compressible turbulence: the cascade and its locality. *Phys. Rev. Lett.* **106** (17), 174502.

ALUIE, H. 2013 Scale decomposition in compressible turbulence. *Physica* D **247**, 54–65.

BESNARD, D. 2007 The megajoule laser programignition at hand. *Eur. Phys. J.* D **44**, 207–213.

BIAN, X., ALUIE, H., ZHAO, D., ZHANG, H. & LIVESCU, D. 2020 Revisiting the late-time growth of single-mode rayleigh–taylor instability and the role of vorticity. *Physica* D **403**, 132250.

BODNER, S. E., COLOMBANT, D. G., GARDNER, J. H., LEHMBERG, R. H., OBENSCHAIN, S. P., PHILLIPS, L., SCHMITT, A. J., SETHIAN, J. D., MCCRORY, R. L., SEKA, W., *et al.* 1998 Direct-drive laser fusion: status and prospects. *Phys. Plasmas* **5**, 1901–1918.

BOFFETTA, G. & MAZZINO, A. 2017 Incompressible Rayleigh–Taylor turbulence. *Annu. Rev. Fluid Mech.* **49**, 119–143.

BOFFETTA, G., MAZZINO, A., MUSACCHIO, S. & VOZELLA, L. 2009 Kolmogorov scaling and intermittency in Rayleigh–Taylor turbulence. *Phys. Rev.* E **79**, 065301(R).

CABOT, W. 2006 Comparison of two- and three-dimensional simulations of miscible Rayleigh–Taylor instability. *Phys. Fluids* **18** (4), 045101.

CABOT, W. H. & COOK, A. W. 2006 Reynolds number effects on Rayleigh–Taylor instability with possible implications for type Ia supernovae. *Nature Phys.* **2** (8), 562–568.

CABOT, W. & ZHOU, Y. 2013 Statistical measurements of scaling and anisotropy of turbulent flows induced by Rayleigh–Taylor instability. *Phys. Fluids* **25** (1), 015107.

CAPRONI, A., LANFRANCHI, G. A., DA SILVA, A. L. & FALCETA-GONÇALVES, D. 2015 Three-dimensional hydrodynamical simulations of the supernovae-driven gas loss in the dwarf spheroidal galaxy Ursa minor. *Astrophys. J.* **805**, 109.

CELANI, A., MAZZINO, A. & VOZELLA, L. 2006 Rayleigh–Taylor turbulence in two dimensions. *Phys. Rev. Lett.* **96** (13), 134504.

CHERTKOV, M. 2003 Phenomenology of Rayleigh–Taylor turbulence. *Phys. Rev. Lett.* **91** (11), 115001.

CHERTKOV, M., LEBEDEV, V. & VLADIMIROVA, N. 2009 Reactive Rayleigh–Taylor turbulence. *J. Fluid Mech.* **633**, 1–16.

CHU, Y.-B. & LU, X.-Y. 2013 Topological evolution in compressible turbulent boundary layers. *J. Fluid Mech.* **733**, 414–438.

CLARK, T. T. 2003 A numerical study of the statistics of a two-dimensional Rayleigh–Taylor mixing layer. *Phys. Fluids* **15**, 2413–2423.

COOK, A. W. & ZHOU, Y. 2002 Energy transfer in Rayleigh–Taylor instability. *Phys. Rev.* E **66**, 026312.

DALZIEL, S. B., LINDEN, P. F. & YOUNGS, D. L. 1999 Self-similarity and internal structure of turbulence induced by Rayleigh–Taylor instability. *J. Fluid Mech.* **399**, 1–48.

DIMOTAKIS, P. E. 2000 The mixing transition in turbulent flows. *J. Fluid Mech.* **409**, 69–98.

GAUTHIER, S. 2017 Compressible Rayleigh–Taylor turbulent mixing layer between Newtonian miscible fluids. *J. Fluid Mech.* **830**, 211–256.

GEORGE, E. & GLIMM, J. 2005 Self-similarity of Rayleigh–Taylor mixing rates. *Phys. Fluids* **17** (5), 054101.

HINDS, W. C., ASHLEY, A., KENNEDY, N. J. & BUCKNAM, P. 2002 Conditions for cloud settling and Rayleigh–Taylor instability. *Aerosol Sci. Technol.* **36**, 1128–1138.

JIANG, G.-S. & SHU, C.-W. 1996 Efficient implementation of weighted ENO schemes. *J. Comput. Phys.* **126**, 202–228.

JIN, H., LIU, X.-F., LU, T., CHENG, B., GLIMM, J. & SHARP, D. H. 2005 Rayleigh–Taylor mixing rates for compressible flow. *Phys. Fluids* **17** (2), 024104.

KORD, A. & CAPECELATRO, J. 2019 Optimal perturbations for controlling the growth of a Rayleigh–Taylor instability. *J. Fluid Mech.* **876**, 150–185.

LAFAY, M.-A., LE CREURER, B. & GAUTHIER, S. 2007 Compressibility effects on the Rayleigh–Taylor instability between miscible fluids. *Europhys. Lett.* **79**, 64002.

LE CREURER, B. & GAUTHIER, S. 2008 A return toward equilibrium in a 2D Rayleigh–Taylor instability for compressible fluids with a multidomain adaptive Chebyshev method. *Theor. Comput. Fluid Dyn.* **22**, 125–144.

LEES, A. & ALUIE, H. 2019 Baropycnal work: a mechanism for energy transfer across scales. *Fluids* **4** (2), 92.

LI, H.-F., HE, Z.-W., ZHANG, Y.-S. & TIAN, B.-L. 2019 On the role of rarefaction/compression waves in Richtmyer–Meshkov instability with reshock. *Phys. Fluids* **31** (5), 054102.

MATSUMOTO, T. 2009 Anomalous scaling of three-dimensional Rayleigh–Taylor turbulence. *Phys. Rev.* E **79** (5), 055301.

MELLADO, J. P., SARKAR, S. & ZHOU, Y. 2005 Large-eddy simulation of Rayleigh–Taylor turbulence with compressible miscible fluids. *Phys. Fluids* **17**, 076101.

MOMENI, M. 2013 Linear study of Rayleigh–Taylor instability in a diffusive quantum plasma. *Phys. Plasmas* **20**, 082108.

NOVAK, G. S., OSTRIKER, J. P. & CIOTTI, L. 2011 Feedback from central black holes in elliptical galaxies: two-dimensional models compared to one-dimensional models. *Astrophys. J.* **737**, 26.

OLSON, B. J. & COOK, A. W. 2007 Rayleigh–Taylor shock waves. *Phys. Fluids* **19** (12), 128108.

QIU, X., LIU, Y.-L. & ZHOU, Q. 2014 Local dissipation scales in two-dimensional Rayleigh–Taylor turbulence. *Phys. Rev.* E **90**, 043012.

RECKINGER, S. J., LIVESCU, D. & VASILYEV, O. V. 2012 Simulations of compressible Rayleigh–Taylor instability using the adaptive wavelet collocation method. In *Seventh International Conference on Computational Fluid Dynamics (ICCFD7), Big Island, Hawaii*.

RECKINGER, S. J., LIVESCU, D. & VASILYEV, O. V. 2016 Comprehensive numerical methodology for direct numerical simulations of compressible Rayleigh–Taylor instability. *J. Comput. Phys.* **313**, 181–208.

SCHNEIDER, N. & GAUTHIER, S. 2016 Vorticity and mixing in Rayleigh–Taylor Boussinesq turbulence. *J. Fluid Mech.* **802**, 395–436.

VLADIMIROVA, N. & CHERTKOV, M. 2009 Self-similarity and universality in Rayleigh–Taylor, Boussinesq turbulence. *Phys. Fluids* **21**, 015102.

WANG, L. & LU, X.-Y. 2012 Flow topology in compressible turbulent boundary layer. *J. Fluid Mech.* **703**, 255–278.

WANG, J.-C., WAN, M.-P., CHEN, S. & CHEN, S.-Y. 2018 Kinetic energy transfer in compressible isotropic turbulence. *J. Fluid Mech.* **841**, 581–613.

WANG, J.-C., YANG, Y.-T., SHI, Y.-P., XIAO, Z.-L., HE, X.-T. & CHEN, S.-Y. 2013 Cascade of kinetic energy in three-dimensional compressible turbulence. *Phys. Rev. Lett.* **110**, 214505.

WIELAND, S. A., HAMLINGTON, P. E., RECKINGER, S. J. & LIVESCU, D. 2019 Effects of isothermal stratification strength on vorticity dynamics for single-mode compressible Rayleigh–Taylor instability. *Phys. Rev. Fluids* **4** (9), 093905.

YEUNG, P. K. & POPE, S. B. 1989 Lagrangian statistics from direct numerical simulations of isotropic turbulence. *J. Fluid Mech.* **207**, 531–586.

YOUNGS, D. L. 1984 Numerical simulation of turbulent mixing by Rayleigh-Taylor instability. *Physica* D **12**, 32–44.

YOUNGS, D. L. 1991 Three-dimensional numerical simulation of turbulent mixing by Rayleigh–Taylor instability. *Phys. Fluids* A **3**, 1312–1320.

YU, J.-L. & LU, X.-Y. 2019 Topological evolution near the turbulent/non-turbulent interface in turbulent mixing layer. *J. Turbul.* **20**, 300–321.

YU, J.-L. & LU, X.-Y. 2020 Subgrid effects on the filtered velocity gradient dynamics in compressible turbulence. *J. Fluid Mech.* **892**, A24.

ZHOU, Y. 2001 A scaling analysis of turbulent flows driven by Rayleigh–Taylor and Richtmyer–Meshkov instabilities. *Phys. Fluids* **13** (2), 538–543.

ZHOU, Q. 2013 Temporal evolution and scaling of mixing in two-dimensional Rayleigh–Taylor turbulence. *Phys. Fluids* **25**, 085107.

ZHOU, Y. 2017a Rayleigh–Taylor and Richtmyer–Meshkov instability induced flow, turbulence, and mixing. I. *Phys. Rep.* **720**, 1–136.

ZHOU, Y. 2017b Rayleigh–Taylor and Richtmyer–Meshkov instability induced flow, turbulence, and mixing. II. *Phys. Rep.* **723**, 1–160.

ZHOU, Q., HUANG, Y.-X., LU, Z.-M., LIU, Y.-L. & NI, R. 2016 Scale-to-scale energy and enstrophy transport in two-dimensional Rayleigh–Taylor turbulence. *J. Fluid Mech.* **786**, 294–308.

ZHOU, Z.-R., ZHANG, Y.-S. & TIAN, B.-L. 2018 Dynamic evolution of Rayleigh–Taylor bubbles from sinusoidal, W-shaped, and random perturbations. *Phys. Rev.* E **97** (3), 033108.

ZWEIBEL, E. 1991 Spinning a tangled web. *Nature* **352**, 755–756.